

1 **Stresses in the lunar interior: insights from slip**
2 **directions in the A01 deep moonquake nest**

3 **A. R. Turner ¹, J.C. Hawthorne ¹ and M. Gaddes ²**

4 ¹Department of Earth Sciences, University of Oxford, Oxford, UK

5 ²COMET, University of Leeds, Leeds, UK

6 **Key Points:**

- 7 • We examine why some moonquakes appear to slip in the opposite direction from
8 the others
9 • Using moonquake waveforms, we infer that slip direction changes through time
10 because of tidal loading
11 • The results indicate that the tidal stress, with magnitude 0.1 MPa, is larger than
12 the tectonic stress

Corresponding author: Alice Turner, alice.turner@earth.ox.ac.uk

Abstract

We probe the present-day stresses in the lunar interior by examining the slip directions of moonquakes in the A01 nest. In this nest, some deep moonquakes appear to slip “backwards”, in the opposite direction to other events. We assess whether these changes in slip direction result from a spatial variation in the tectonic stress or from a temporal variation in the tidal stress. To test these two options, we first show that a dominant tectonic stress implies deep moonquakes can only slip in one direction: forwards and backwards, while a dominant tidal stress could allow moonquakes to slip in more directions: any combination of forwards, backwards, left, and right. Then we look for the number of slip directions; we separate the deep moonquake waveforms into slip directions using a principal component analysis technique. We find two slip directions present in the A01 deep moonquake nest. The moonquakes slip in a variety of directions as time evolves. This observation implies that the tidal stresses drive deep moonquakes. Additionally, these results place a new constraint on the magnitude of the tectonic stresses at depth; they must be smaller than the modelled tidal stress of ~ 0.1 MPa.

Plain Language Summary

The stresses that act in the lunar interior are not well known but are important for improving our knowledge of the interior of the Moon and its evolution. Deep inside the Moon, at depths between 700 km and 1200 km, moonquakes occur approximately every 27 days, suggesting they are influenced by the tides. Are the tides responsible for generating deep moonquakes? Or is long-term tectonic stress, in addition to the tidal stresses responsible? Using the waveforms of these deep moonquakes, we aim to determine the relative magnitudes of the tidal and tectonic stresses acting deep in the lunar interior. To do this, we look at the directions in which the moonquakes slip. We observe that deep moonquakes slip in a variety of different directions, which can only be caused by tidal stresses. Since these deep moonquakes are generated by the tides, this observation reveals that tectonic stresses in the lunar interior must be smaller than 0.1 MPa.

1 introduction

During the Apollo missions in the 1970s, four seismic stations were placed on the Moon’s near side. These seismic stations recorded hundreds of deep moonquakes, which occur at depths of 700 - 1200 km.

Deep moonquakes tend to occur in clusters called “nests”. In each nest, moonquakes occur at monthly intervals; they are seemingly influenced by the Earth-induced tidal stresses (Lammlin, 1977; Toksöz et al., 1977; Nakamura, 1978; Minshull & Gouly, 1988; Weber et al., 2009, 2010). However, the details of that influence remain unclear. Do tides trigger deep moonquakes by adding a small perturbation in stress on top of a large long-term tectonic stress? Or do tides generate deep moonquakes by providing most or all the stress at depth? Here we aim to resolve the role of tidal stresses in driving deep moonquakes and to constrain the relative magnitudes of tidal and tectonic stresses.

Some previous observations suggest that tidal stresses dominate the stress field in the deep moonquake source region. The tidal stress is large enough to account for the entire stress released in deep moonquakes (Kawamura et al., 2017). And large tidal stresses could also explain why some moonquakes appear to slip “backwards”: in the opposite directions of most moonquakes in the nest. Moonquake slip directions could reverse if the tidal stresses dominate the local stress field and allow a reversal in the stress direction over their monthly oscillations (Toksöz et al., 1977; Nakamura, 1978).

However, other observations suggest that tectonic stresses dominate the local stress field. The tidal stresses may be larger than moonquake stress release, but local confin-

ing stresses are 10,000 times larger still (Minshull & Gouly, 1988). Additionally, deep moonquakes must respond to some non-tidal stress, as they do not always occur when the tangential tidal stress is the highest (Araki, 2001; Weber et al., 2009).

1.1 Motivation

1.1.1 Insights for the lunar interior

If tectonic stresses dominate the local stress field, they could have a variety of origins. They could be elastic stresses preserved from early lunar events (Weber et al., 2009); stresses generated by continuing weak convection (Frohlich & Nakamura, 2009); thermal stress from contraction of the lunar interior as it cools (Minshull & Gouly, 1988; Solomon & Chaiken, 1976); volumetric stresses from phase changes (Weber et al., 2009); or stresses concentrated around compositional heterogeneities within the lunar interior (Zhao et al., 2012; Qin et al., 2012; Sakamaki et al., 2010; Steinberger et al., 2015). There are, however, few observational constraints on the stresses involved in these processes (Solomon & Chaiken, 1976). We may better constrain the long term stress magnitudes by understanding the stresses that drive deep moonquakes.

1.1.2 Deep moonquake mechanisms

Understanding the stresses in the lunar interior may also help us understand deep moonquakes themselves. These ruptures are enigmatic; they occur at pressures of ~ 4 GPa and temperatures of 1500 to 1600 K (Kawamura et al., 2017), where rocks are expected to deform slowly and ductilely, not in abrupt brittle failures.

Three mechanisms are commonly proposed to explain the existence of deep moonquakes: the same mechanisms proposed to generate intermediate-depth (~ 100 km) and deep (> 410 km) earthquakes. Deep moonquakes may occur via (1) increased pore fluid pressure, which decreases the effective normal stress and allows for brittle failure at greater depths (e.g., Davies, 1999; Meade & Jeanloz, 1991; Hacker et al., 2003; Proctor & Hirth, 2015; Brantut et al., 2011; Dobson et al., 2002). Alternatively, they may occur via (2) thermal runaway, where a large initial shear stress and a small increase in strain rate lead to heating, runaway weakening and failure (e.g., Ogawa, 1987; Karato et al., 2001; Kelemen & Hirth, 2007; John et al., 2009; Thielmann et al., 2015; Thielmann, 2018). Or finally, moonquakes may occur via (3) a volume change and faulting associated with a mineralogical phase change (e.g., Kirby et al., 1996; Kirby, 1987; Green & Burnley, 1989; Burnley et al., 1991; Schubnel et al., 2013).

1.2 Models of reversed polarity moonquakes

In our search for the relative magnitudes of the tidal and tectonic stresses in the moonquake source region, we will focus on the stresses that allow reversed polarity moonquakes. Reversed polarity moonquakes generate waveforms similar to the waveforms of normal-polarity moonquakes, just flipped (Figure 1a). These reversed polarity waveforms were observed at the A01 deep moonquake nest in 1972, 1973 and 1974, interspersed with normal polarity waveforms (Nakamura, 1978). They originate from the same location as the normal polarity moonquakes but imply that some moonquakes in this location slip in the opposite direction to the rest. We test two models to explain this slip reversal.

1.2.1 Tectonic plug model

In the first proposed model, the long-term tectonic stress is larger than the oscillatory tidal stress. The shear stress at a given location is thus always in the same direction (arrows in Figure 1b). However, the stress may vary in space. Slip may occur on two parallel shear zones on either side of a moving plug, as sometimes observed during

107 volcanic dyke intrusions (White et al., 2011). The motion of the plug would produce moon-
 108 quakes that slip in roughly opposite directions, as observed.

109 **1.2.2 Tidal model**

110 In the second proposed model, first suggested by Nakamura (1978), the oscillatory
 111 tidal stress is larger than the long-term tectonic stress. The stress direction can thus vary
 112 with time on a fixed fault plane (Figure 1c). Reversed polarity moonquakes can occur
 113 on the same fault plane as normal moonquakes.

114 **1.2.3 Differentiating between models for apparent slip reversal in the** 115 **A01 nest**

116 To test these models, we note that in the plug model, the stress is either forwards
 117 or backwards; there is one stress direction for each side of the plug. But in the tidal model,
 118 the stress can also rotate to different rakes along the fault plane (from the green to the
 119 blue arrow in Figure 1c). Since faults slip in the direction of the stress, we can make a
 120 similar statement about moonquake slip directions. In the plug model, moonquakes can
 121 slip forwards and backwards, but in the tidal model, moonquakes can slip in 2-D space,
 122 with any combination of left, right, forwards, and backwards.

123 We aim to determine whether the normal and reversed polarity moonquakes in the
 124 A01 nest slip along one direction (forwards and backwards) or along two directions (left,
 125 right, forwards, and backwards) and thus identify the dominant stress generating deep
 126 moonquakes. To do so, we will separate the energy in the deep moonquake waveforms
 127 into one or more slip directions with a principal component analysis (PCA) approach.
 128 We will apply a range of statistical tests to assess the slip directions' robustness.

129 **2 Data Selection and Initial Processing**

130 In this study, we focus on the A01 deep moonquake nest. The nest is located 18°
 131 southwest of station S12 at a depth of 870 km (Nakamura, 2005) and is the most active
 132 moonquake nest, providing enough good quality data to determine the number of slip
 133 directions.

134 We download the 3-component long period Apollo seismic data from the GEOSCOPE
 135 observatory through the IGP data center (<http://datacenter.ipgp.fr/>). The original data
 136 was stored on magnetic tape, but it has been extracted from binary to SEED format for
 137 easier access (Nunn et al., 2017; Nunn, Weber, & Panning, 2020). The data were recorded
 138 in two instrument response modes, flat and peaked mode. The peaked instrument re-
 139 sponse mode was the natural response of the seismometer, with a peak in the frequency
 140 response at about 0.45 Hz (Nunn, Garcia, et al., 2020). The flat instrument mode was
 141 designed to be sensitive to a broader frequency range, from about 0.1 to 1 Hz (Nunn,
 142 Garcia, et al., 2020). We consider moonquakes recorded in the two instrumental modes
 143 and at each station separately, so we leave the data as they were recorded and do not
 144 deconvolve the instrument response.

145 To identify A01 moonquakes, we use the Nakamura (2003) catalogue with updates
 146 from Bulow et al. (2005). We assess the waveforms by eye to include only moonquakes
 147 with clear onsets and good signal to noise ratios.

148 We found few good quality moonquakes with clear arrivals at stations S14 or S15
 149 and therefore analyse data from stations S12 and S16 only. Figure 2 illustrates the wave-
 150 forms recorded in peaked mode on the north channel (MHN) of station S12. Figures s.1
 151 - s.7 illustrate waveforms recorded on the east channel (MHE), in flat mode, and at sta-
 152 tion S16.

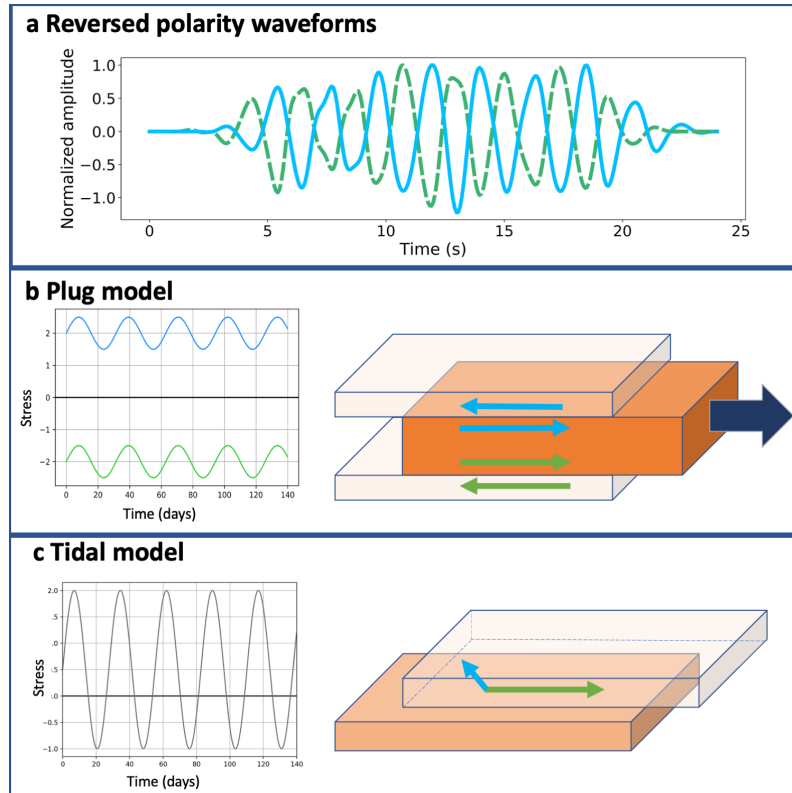


Figure 1. (a) A pair of moonquakes with reversed polarities, recorded on the east channel of station S16. The blue waveform was recorded on 17th November 1973, and the green waveform was recorded on 5th October 1975. Two models have been proposed to explain the reversed polarity waveforms. In (b) the plug model, the long-term tectonic stress is larger than the oscillatory tidal stress. The stress directions (arrows) are constant in time but change from one side of the plug to the other. In (c) the tidal model, the tidal stress is larger than the tectonic stress. Slip occurs on a single fault plane, and the stress direction (arrows) changes over time, assuming a range of rakes.

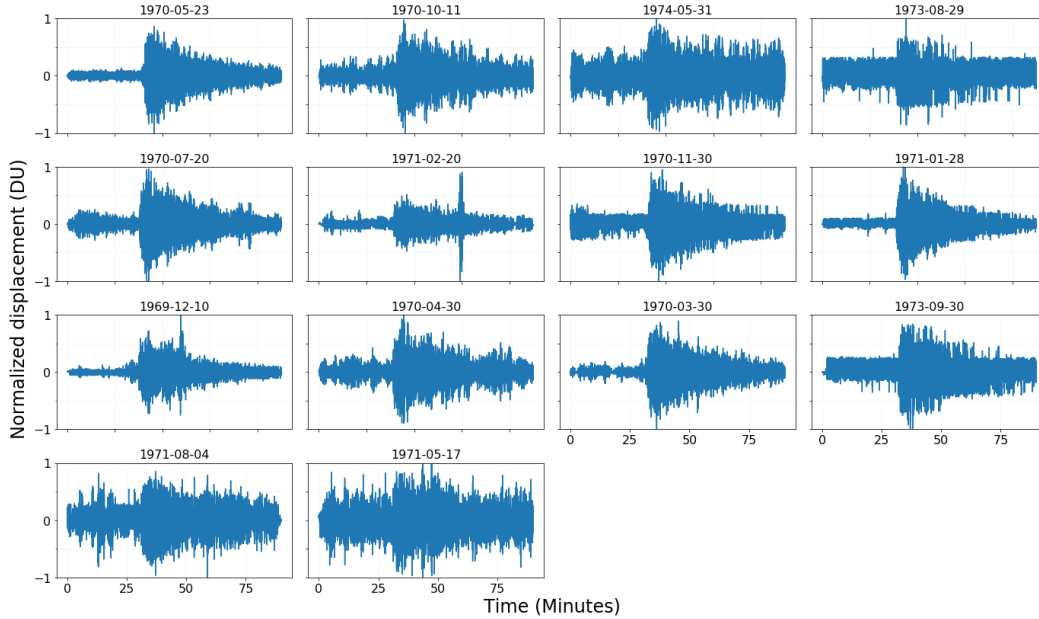


Figure 2. Deep moonquake waveforms used for PCA decomposition, recorded at station S12, channel MHN, in the peaked operation mode.

3 Principal component analysis of A01 moonquake waveforms

To assess the stress state in the deep moonquake generating region, we examine moonquake slip directions using a principal component analysis, a method not regularly used on earthquakes. For terrestrial problems, researchers often determine individual earthquake’s focal mechanisms—their fault planes and slip directions—using the polarities of first arrivals recorded at a number of stations (e.g., Hardebeck & Shearer, 2002; Yang et al., 2012). However, moonquake slip directions cannot be estimated with those techniques; moonquake seismograms have emergent onsets, as shown in Figure 2 and are recorded at only four stations (Nakamura, 1978; Weber et al., 2009).

Instead, then, we determine the range of moonquake slip directions by comparing waveforms of various events in the A01 nest. Let us consider all the A01 moonquake seismograms $U_k(t)$ recorded on a single channel at a single station. Since the moonquakes in a nest occur within a compact cluster, only a few km wide (Nakamura, 1978), we can model the displacement at the lunar surface created by the moonquake as :

$$U_k(t) = \sum_{j=1}^J G_j(t) m_{jk}, \quad (1)$$

as illustrated in Figure 3. Here U_k is the waveform for event k , and G_j is the Green’s function: the surface displacement produced by unit moment (slip times area times local shear modulus) in direction j . We call m_{jk} the slip coefficient: it is the moment in direction j for event k .

If we collect the waveforms $U_k(t)$ observed from several A01 moonquakes k into the columns of the matrix \mathbf{U} , we may note that Equation 1 has the same form as that used in the principal component analysis: $\mathbf{U} = \mathbf{G}\mathbf{m}$. PCA decomposes the data matrix (\mathbf{U}) into a set of coefficients (rows of \mathbf{m}) multiplied by a set of basis vectors or principal components (columns of \mathbf{G}). It would thus seem that we can use a PCA decomposition to

176 recover the slip coefficients (\mathbf{m}) and Green’s functions (\mathbf{G}) from the deep moonquake wave-
177 forms.

178 However, it is important to note that the PCA decomposition always recovers the
179 same number of principal components as waveforms. The components are chosen such
180 that the first components accommodate as much of the signal in the data vectors U_k as
181 as possible. Later components accommodate progressively less signal. We expect the first
182 few principal components to be Green’s functions for the slip in one or more directions,
183 as they can accommodate signal from multiple moonquakes. Later principal components
184 are likely to be noise, which differs from event to event. Our challenge will be to deter-
185 mine which principal components represent Green’s functions and which principal com-
186 ponents represent noise.

187 The number of principal components representing Green’s functions will let us dis-
188 tinguish between the two models of moonquake slip presented in section 1.1. For the plug
189 model, we hypothesise that there is a single slip direction; one direction should have a
190 large m_1 and contain signal common to multiple moonquakes, while all other m_k should
191 be close to zero. In contrast, the tidal model predicts two slip directions; two directions
192 should have a large m_1 and m_2 , and all other m_k should be close to zero.

193 In carrying out the PCA, we must ensure good waveform alignment. The signal
194 in each principal component is sensitive to waveform alignment, as time-shifted traces
195 can be mapped into different components. Before we compute the PCA decomposition,
196 we cross-correlate each waveform with a high-quality template event to obtain a best-
197 fitting initial time shift, as described in section 2. Then we apply the principal compo-
198 nent analysis to a 10-minute window of the A01 deep moonquake waveforms, which in-
199 cludes the direct P and S arrivals and scattered arrivals in the coda. Finally, we ensure
200 the best alignment between the waveforms by searching 0.7 s (10 samples) around the
201 cross-correlation time shifts to maximise the energy in the first component of the PCA.

202 The Green’s functions determined from the PCA decomposition are plotted in Fig-
203 ure 4. We discuss their qualitative characters in section 4. In section 5, we examine the
204 slip coefficients and principal components more quantitatively.

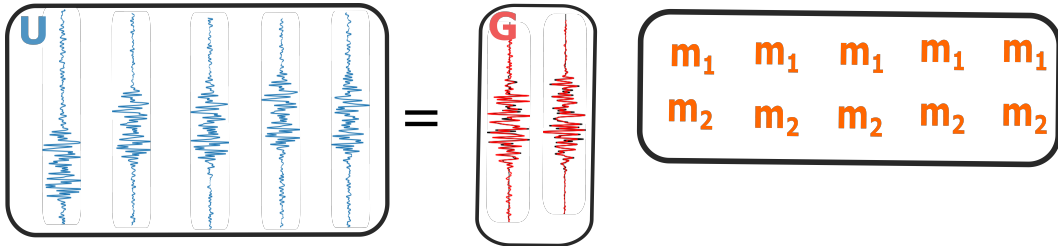


Figure 3. Illustration of the PCA decomposition for the A01 moonquakes into two slip direc-
tions. A matrix of waveforms (blue, \mathbf{U}), is decomposed into the Green’s Functions (red, \mathbf{G}), and
the slip coefficients (orange, \mathbf{m}) for each of the two slip directions illustrated. The later compo-
nents also recovered in the PCA are not illustrated.

205 4 Qualitative analysis of the principal components (\mathbf{G})

206 Figure 4 shows the 14 principal components for the peaked mode MHN records at
207 station S12, ordered by the percentage of the data variance they explain. The first three
208 principal components, which explain the most variance, have clear onsets in signal fol-
209 lowed by decays. They have “moonquake-like” shapes, similar to the waveforms in Fig-

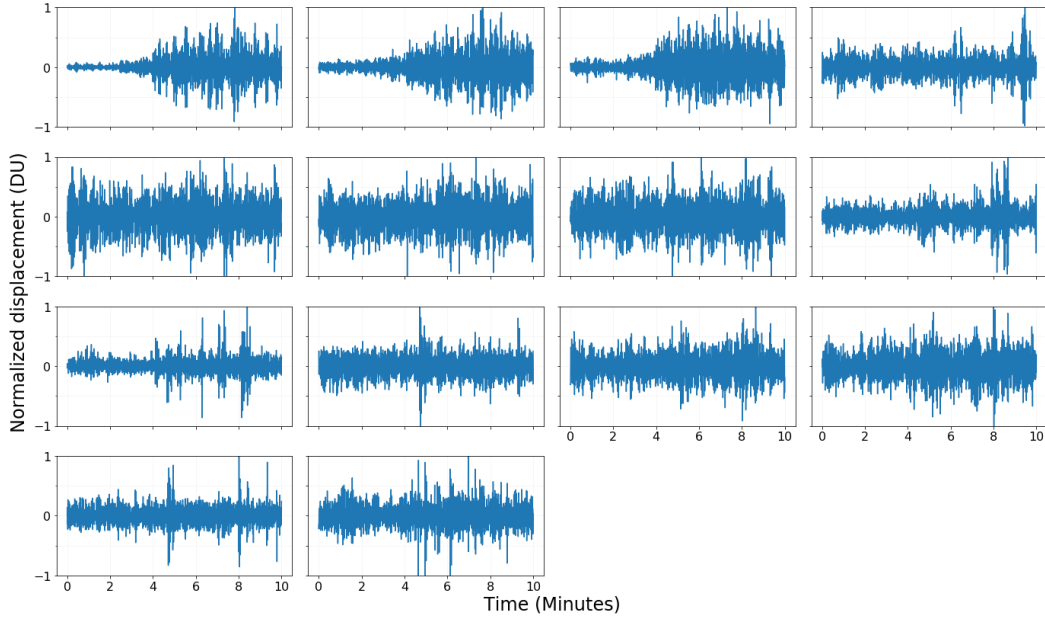


Figure 4. Principal components derived from the S12 MHN data in the peaked operational mode of the instrument.

210 ure 2. These shapes suggest that the first three principal components could represent
 211 real Green’s functions. Later principal components, which explain progressively less of
 212 the variance, do not have clear onsets or decaying “moonquake-like” shapes.

213 Using the MHE records at station S12 (Figure s.8), we also observe three moonquake-
 214 shaped principal components. However, when we analyse the flat mode MHN and MHE
 215 data (Figures s.9 and s.10), there are only two “moonquake-shaped” principal compo-
 216 nents.

217 When we analyse the waveforms recorded at station S16 (Figures s.11 - s.14), we
 218 again observe three moonquake-shaped components in the decomposition of the peaked
 219 mode data and two moonquake-shaped components in the flat mode data. A qualita-
 220 tive analysis of all the data thus suggests that two or three principal components rep-
 221 resent Green’s functions, while the rest represent noise.

222 5 Quantitative analysis of the number of slip directions

223 Next, we aim to more rigorously determine whether each derived principal compo-
 224 nent represents a Green’s function or represents noise. We quantitatively analyse the
 225 “slip” coefficients m obtained for each principal component and event (section 5.1) as
 226 well as the principal component vectors G themselves (section 5.2).

227 5.1 Determining number of slip directions using unbiased principal com- 228 ponent coefficients (m’)

229 The “slip” coefficients m_{jk} determine how much of each principal component j is
 230 needed to reconstruct the seismogram generated by moonquake k . If a principal com-
 231 ponent $G_j(t)$ represents a real Green’s function, its coefficients are likely to be large for
 232 multiple moonquakes k . We therefore aim to assess the coefficients’ values.

233 To accurately assess the coefficients' values, we need to compare the principal com-
 234 ponent vectors with “unseen” validation waveforms. We want to know how well each prin-
 235 cipal component can be used to reconstruct moonquake waveforms that were not em-
 236 ployed in creating the principal component vectors.

237 To achieve this, we use a method similar to “leave-one-out cross-validation” (Bishop
 238 & Nasrabadi, 2006). We calculate the PCA using all but one “left-out” moonquake wave-
 239 form. We project the left-out waveform onto each of the principal components to obtain
 240 an unbiased coefficient m'_{jk} for component j and moonquake k :

$$m'_{jk} = G_{res,j}(t) \bullet u_k(t). \quad (2)$$

241 Here u_k is the waveform of the excluded moonquake, and $G_{res,j}$ is the j th princi-
 242 pal component, calculated using the remaining moonquakes. We repeat this process, ex-
 243 cluding each available moonquake k in turn, so that we have a set of unbiased coefficients
 244 m'_{jk} for each moonquake.

245 We use a bootstrap approach to estimate the uncertainty on the coefficients m'_{jk} .
 246 We again exclude event k and recompute the principal components, but instead of us-
 247 ing all remaining moonquakes in the PCA calculation, we randomly choose 20 of the re-
 248 maining moonquakes with replacement. With this new subset of moonquakes, we recom-
 249 pute the principal components $G_{res,j}$ and the projected coefficients m'_{jk} 25 times.

250 The coloured circles in Figure 5b-d show these 25 projected coefficients m'_{jk} for each
 251 of the station S12 MHN moonquakes. The coefficient for the first principal component
 252 m'_{i1} is plotted on the x-axis. The coefficients of the second (m'_2), third (m'_3), and twenti-
 253 eth (m'_{20}) principal components are plotted on the y axis of panels b,c and d, respec-
 254 tively. Each event k is plotted in a different colour.

255 Figure 5a summarises the distribution of the coefficients of the first principal com-
 256 ponent m_1 for all moonquakes from the peaked mode S12 data. The distribution of the
 257 coefficients is bi-modal, with clusters around ± 12 . Note that a single event can have both
 258 a positive and negative m' because the signs of G_i and m'_i can trade-off; in bootstrap-
 259 ping, G_i can flip and be compensated by a flip in the sign of m'_i . The non-zero average
 260 amplitude of the coefficients, along with the gap around zero, implies that there is a large
 261 m'_1 common to all moonquakes. The first principal component thus seems to represent
 262 a real Green's function.

263 Panel e summarises the distribution of the coefficients of the second principal com-
 264 ponent, m'_2 . The bi-modal distribution and non-zero average amplitude of the coefficients
 265 that imply the second principal component also represents a real Green's function.

266 Panel f and g summarise the distribution of coefficients for the third and twenti-
 267 eth components. These distributions have only a single peak, and the average values of
 268 the distributions are near zero. The near-zero values suggest that there is little moon-
 269 quake signal in these principle components; they mostly accommodate noise that varies
 270 from event to event.

271 We may more quantitatively compare the coefficient distributions with a Kolmogorov-
 272 Smirnov test. We assume that the last (twentieth) principal component accommodates
 273 only noise, and take its coefficient distribution, plotted in panel g, as representative of
 274 the coefficients derived from noise. The first and second principal components' coeffi-
 275 cients differ from this noise distribution with probabilities of near 100% and 99.1%, re-
 276 spectively; these coefficients likely accommodate moonquake signals. In this analysis of
 277 the peaked mode S12 data, the third component's coefficients differ from the noise with
 278 a probability of only 30%. Later components' coefficients are also similar to the distri-
 279 bution of noise.

280 We obtain similar results when we analyse the distribution of coefficients for all other
 281 stations, components, and instrument modes. For example, Figure s.15 summarises the
 282 distribution of coefficients for the station 12 peaked mode MHE waveforms. The distri-
 283 butions of coefficients for the first and second principal components are again bi-modal,
 284 and the average distribution amplitude is non-zero. The distributions differ from noise
 285 with probability near 100 % and 99 %, respectively. The distribution of coefficients in
 286 the third and later slip directions have only a single peak at zero and are similar to the
 287 distribution of coefficients derived from noise.

288 Similar although slightly less well-resolved distributions are obtained from flat mode
 289 data at station S12 (Figure s.16 and s.17). For both the MHN and MHE records, the
 290 distributions of coefficients for the first principal components are bi-modal, and both dif-
 291 fer from noise with probabilities near 100 %. The distributions of the second principal
 292 components are not bi-modal, but they are uniform rather than Gaussian. The distri-
 293 butions still differ from the noise distributions with a probability of 92% and 99% for the
 294 MHN and MHE records. The third principal component also differs from noise with a
 295 probability of 99 %, but it has a large peak at zero. Later components are similar to noise.

296 Similar results are obtained from station S16, as illustrated in Figures s.18 - s.21.
 297 The distributions from all stations and channels imply that two principal components
 298 have a large m'_{jk} common to multiple moonquakes and represent real slip directions.

299 **5.2 Determining number of slip directions using the similarity of the prin-** 300 **cipal component vectors (G)**

301 In the bootstrapping described above, we re-estimated the principal components
 302 G_j and coefficients m'_j for various subsets of the data, and we analysed the coefficients
 303 m'_j . In this section, we examine the variation among the estimated principal component
 304 vectors G_j .

305 We expect little variation in the estimates of a given principal component G_j if that
 306 component recovers a real moonquake signal common to multiple moonquake waveforms.
 307 But we expect large variation in bootstrapped estimates of a principal component G_j
 308 if that principle component recovers noise, which varies between waveforms.

309 We examine the similarity of the bootstrapped principal components using a mod-
 310 ified version of the algorithm ICASAR. This algorithm was originally designed to sep-
 311 arate ground deformation and atmospheric signals in time series of interferograms us-
 312 ing independent component analysis (Gaddes et al., 2019), but we use it to analyse the
 313 similarity of our bootstrapped principal component estimates. The similarity between
 314 two principal component estimates is quantified as the absolute value of their cross-correlations.

315 The ICASAR algorithm clusters the bootstrapped principal components accord-
 316 ing to these cross-correlation values. It uses a hierarchical clustering algorithm (HBD-
 317 SCAN) to identify similar principal component estimates (McInnes et al., 2017; Gaddes
 318 et al., 2019). We assess the quality of clusters using the cluster quality factor I_q : the dif-
 319 ference between the mean intra-cluster similarity (1 for a perfect cluster) and the mean
 320 similarity between members of the cluster and all other component estimates (0 for a per-
 321 fect cluster).

322 We would now like to visualise the similarities between the principal component
 323 estimates, but without plotting the numerous computed cross-correlations. To do so, we
 324 project the set of cross-correlations into a two-dimensional space. We choose the dimen-
 325 sion's directions according to a t-distributed neighbourhood embedding algorithm. These
 326 directions do not have any physical meaning, but they preserve a key feature of distance:
 327 points close together represent component estimates that have a high cross-correlation,

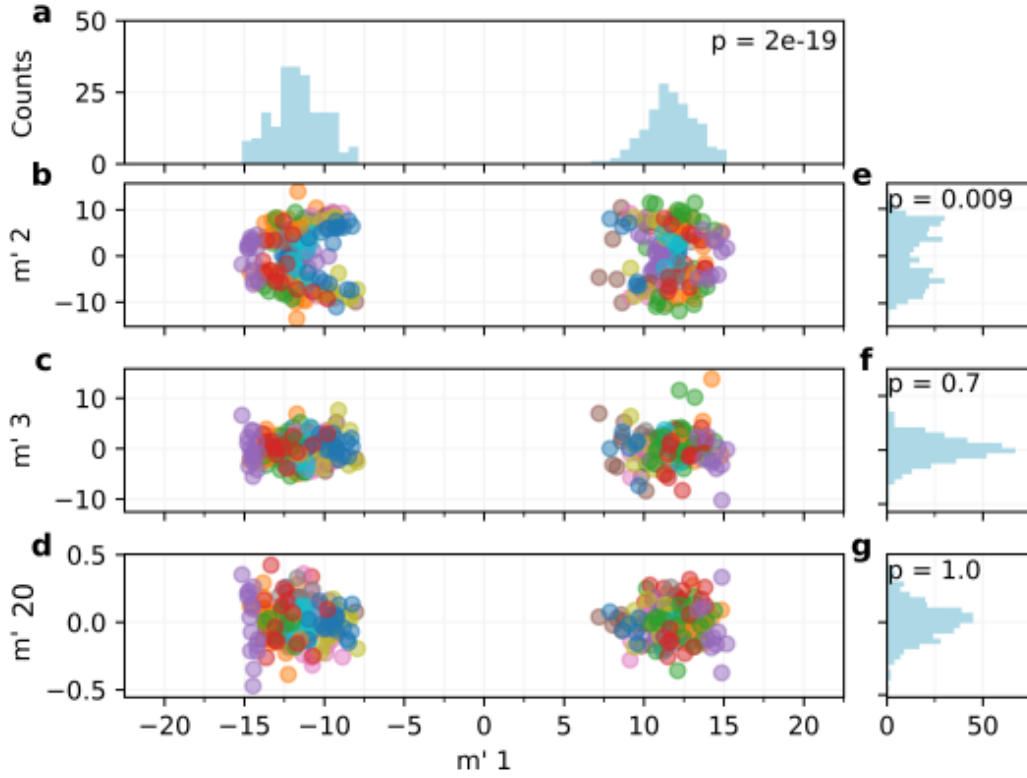


Figure 5. Unbiased coefficients of the principal components, from the S12 MHN data in the peaked operational mode. In panels b-d, the coefficient for the first principal component m'_{i1} is plotted on the x-axis. The coefficients of the second (m'_2), third (m'_3) and twentieth (m'_{20}) principal components are plotted on the y axis of panels b,c and d, respectively. Each event is plotted in a different colour. Panels a, e, f, and g summarise the distribution of coefficients for each of the principal components. The text in the top of panels a, e, f, and g is the probability (p-value) that each distribution differs from the distribution of the coefficients derived from noise. Only the first two components differ from noise.

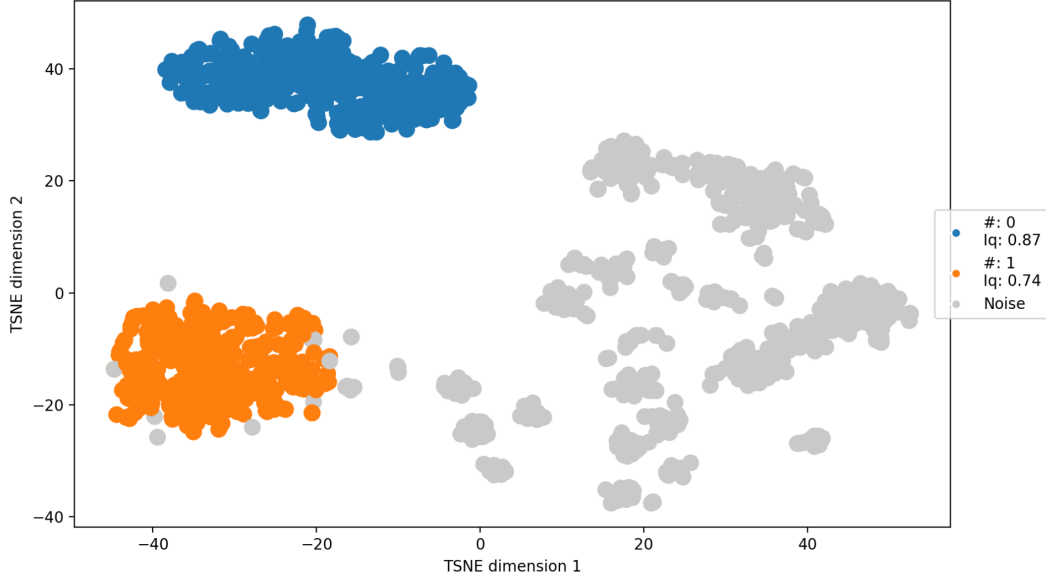


Figure 6. Clustering results of bootstrapped principal component vectors \mathbf{G} , obtained for S12 MHN in peaked operational mode. One point is plotted for each bootstrapped estimate of a principal component, but only the first four principal components are plotted. The location of each point is determined by the t-sne algorithm, preserving the similarity of components from the higher dimensional space (Maaten & Hinton, 2008; Gaddes et al., 2019). The colour of each point is determined by the HBDSCAN clustering algorithm (McInnes et al., 2017; Gaddes et al., 2019). Two clusters are shown, in blue and orange. Grey points represent component estimates that are not assigned to a cluster.

328 while points that are far apart have a low cross-correlation (t-sne, Maaten & Hinton, 2008;
329 Gaddes et al., 2019).

330 Figure 6 shows the clusters determined using principal components of waveforms
331 recorded at station S12 MHN in peaked mode, projected along the first two t-sne direc-
332 tions. Only projections from the first four principal components are shown. Points in
333 Figure 6 are coloured by the clusters identified by the HBDSCAN algorithm. The prin-
334 cipal components estimates in the blue cluster are similar; they have an I_q of 0.87. The
335 estimates in the orange cluster have a slightly lower similarity; $I_q = 0.74$. Points coloured
336 grey represent principal component estimates that are not similar enough to other es-
337 timates to form a cluster.

338 The two clusters identified by the HBDSCAN algorithm and shown visually in Fig-
339 ure 6 suggest that two principal components contain signal common to multiple moon-
340 quakes and that these signals are repeatedly recovered in bootstrapping. We obtain sim-
341 ilar clusters if we adjust the clustering parameters: if we perturb the minimum cluster
342 size or the distance required to define a “neighbour”. Similar clusters are obtained from
343 other stations, components, and instrument modes (Figures s.22-28).

344 5.3 Partitioning of slip between directions

345 Our analysis in sections 5.1 and 5.2 implies that moonquakes in the A01 slip in two
346 directions. We can now analyse the magnitude of slip in each direction, as we can now
347 interpret the first two coefficients m' not just as coefficients of principal components but

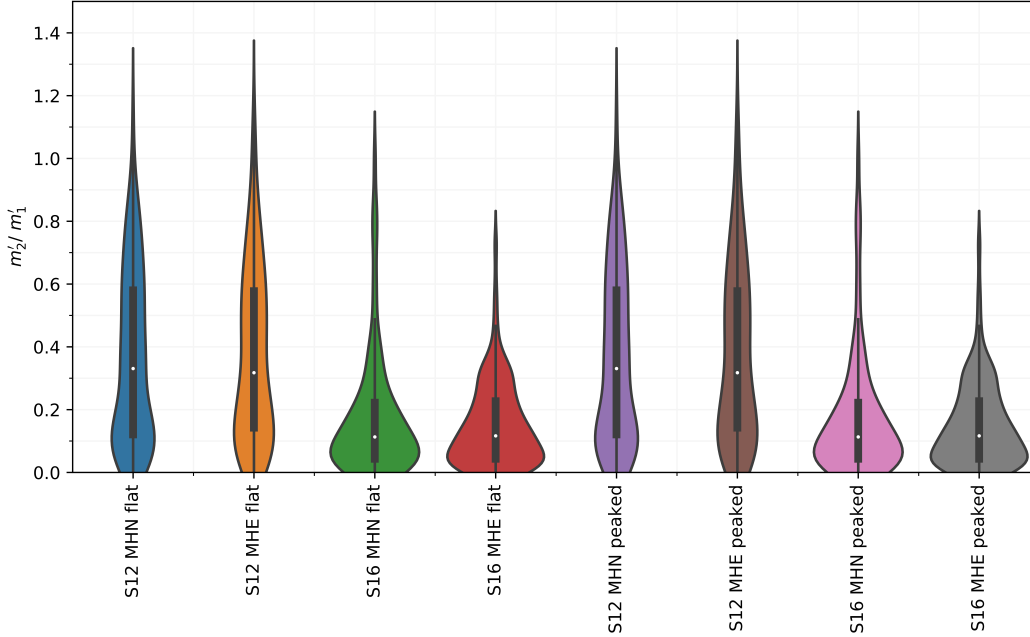


Figure 7. Slip coefficient ratio m'_2/m'_1 for each station and channel. The white dot marks the median bootstrapped ratio at each station, the black bar delimits the interquartile range, and the thin black line delimits $1.5 \times$ the inter-quartile range. The coloured areas illustrate the probability density of the ratio at each station. All distributions have peaks above zero, and the median m'_2/m'_1 ratios range from 0.11 to 0.33.

348 as slip coefficients. Each m'_{jk} is proportional to the amount of moment in each direction
 349 for moonquake k .

350 Figure 7 shows distributions of the $|m'_{1k}/m'_{2k}|$ ratios: the ratio of the moment the
 351 second slip direction to the moment in the first slip direction. These distributions are
 352 also shown plotted on log axis in Figure s.29. The coloured area shows the probability
 353 density of the ratio obtained at each station and component, and the white dots mark
 354 the median ratio. All distributions are consistent with significant slip in the second di-
 355 rection; distributions have peaks above, not at zero, and the median ratios range from
 356 0.11 to 0.33, with a median at all stations of 0.21 .

357 Finally, we can examine how the slip coefficients vary from moonquake to moon-
 358 quake. Figure 8 shows the normalised $m'_i/\sqrt{m_1'^2 + m_2'^2}$ values for peaked mode MHN and
 359 MHE records at stations S12 and S16. If these recovered directions were orthogonal, a
 360 vector from the origin to each point would give the slip direction. Note, however, that
 361 our PCA analysis cannot identify orthogonal slip directions. It only identifies slip di-
 362 rections that produce different Green's functions, and those directions are the ones illus-
 363 trated on the axes of Figure 8.

364 We can nevertheless interpret several features of the varying slip coefficients. First,
 365 Figure 8 shows both positive and negative coefficients in the first slip direction. The neg-
 366 ative coefficients correspond to moonquakes that slip in the opposite direction of most
 367 events; they create the reversed polarity waveforms. Second, and perhaps more inter-
 368 esting, the slip directions do not appear clustered; there is a variable amount of slip in
 369 the second direction. Moonquakes appear to slip in a range of directions within a 2-D
 370 plane, not in two particular directions.

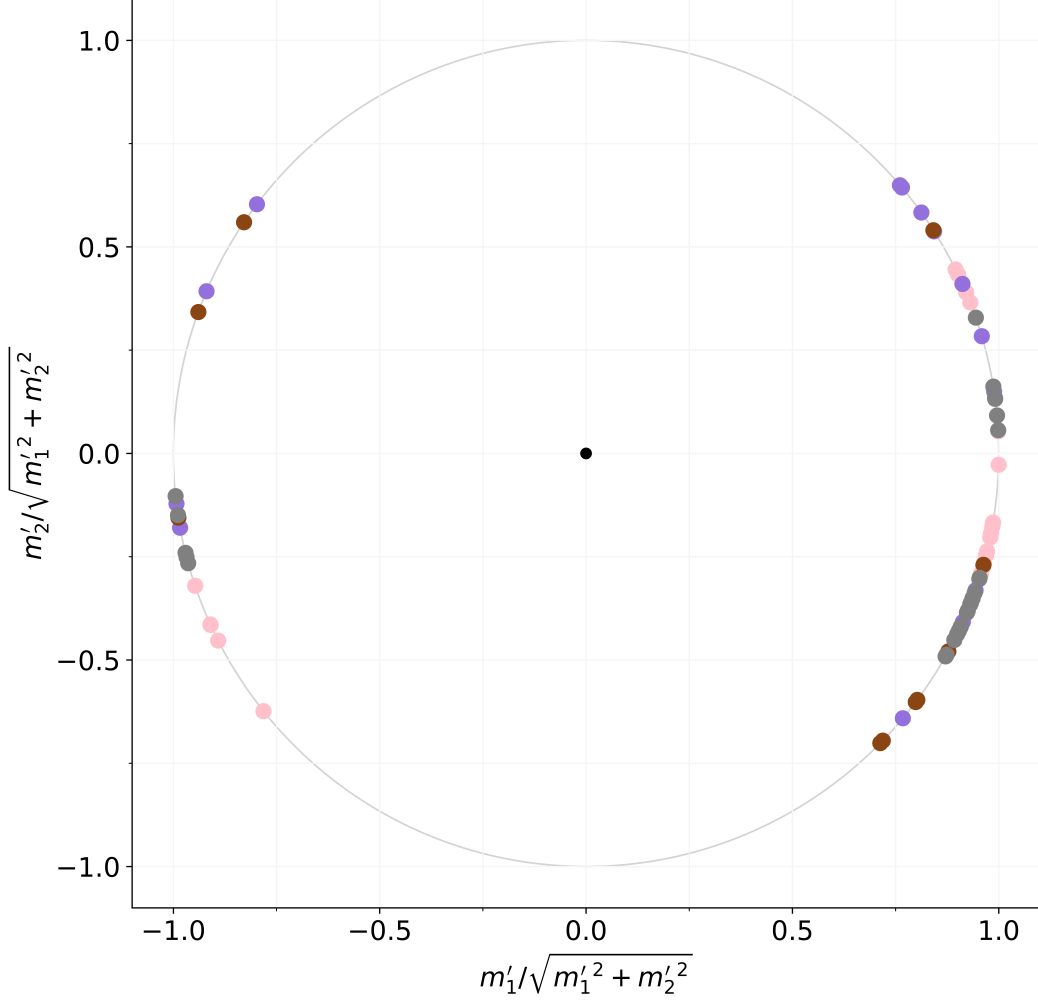


Figure 8. Normalised unbiased slip coefficients for the first and second Green’s functions, for moonquakes recorded at both stations and components in the peaked instrument mode. A vector from each point to the origin would give the slip direction. Negative coefficients in the first slip direction correspond to reversed polarity moonquakes, which slip roughly in the opposite direction of most events. Note, however, that moonquakes appear to slip in a range of direction within the m_1 - m_2 plane. The colours correspond to the station and channel considered, as used in Figure 7 (purple: S12 MHN peaked; brown: S12 MHE peaked; pink: S16 MHN peaked; grey: S16 MHE peaked).

6 Validation

Our analysis implies that two principal components are required to accommodate signal common to many moonquakes in the A01 nest: that these moonquakes slip in two directions. However, some errors have the potential to create artificial principal components. So here we check that the second significant principal component is a physical feature of the moonquakes and not a result of poor waveform alignment (section 6.1) or scattered seismic waves (section 6.2).

6.1 Potential influence of waveform alignment

We first check that we have not obtained two principal components because the moonquake waveforms are poorly aligned. We verify that the second principal component is not a time-shifted version of the first component. Then we examine how the number of significant principal components changes if we add errors in the waveform alignment: if we randomly shift each waveform by a random value drawn from a uniform distribution.

Figure 9 shows the percentage of the variance accommodated by the principal components as we increase the maximum random shift from 0 to 1 second. For shifts up to ~ 0.17 seconds, energy in the first principal component decreases as the alignment worsens, but that energy is distributed over a number of the later components; the energy in the second principal component does not increase significantly. Since our fine-tuning of the time-shift allows an accuracy of 0.07 seconds (the sampling rate of the traces), it seems unlikely that the significant energy we observe in the second principal component results from poor waveform alignment.

6.2 Potential influence of scattering

Next, we assess whether the second slip direction could result from scattering. Moonquakes in the A01 may be in slightly different locations, up to a few km of each other (Nakamura, 2003), and their seismic waves may follow slightly different paths through the Moon, especially in the near-surface scattering layer. The different paths could lead to different recorded seismograms, especially later in the coda, when the seismic waves have been more scattered.

To look for scattering, we apply the PCA to 30-second windows throughout the seismogram, from the direct S wave arrival onward into the coda, as illustrated in Figure 10a. Figure 10b shows the variance explained by the first, second, and twentieth principal components in each of the windows. The different operational modes, components, and stations also give similar results. The variance in the second component does not significantly increase later in the coda, suggesting that scattering later in the coda does not create the significant signal we observe in the second principal component.

7 Discussion

In this study, we have used a PCA approach to separate the signal in deep moonquake waveforms into principal components common to multiple moonquakes. We find that two principal components are required to reconstruct the data. These components likely reflect the signals created by slip in two different directions.

7.1 Explaining reversed polarity moonquakes

We were motivated to examine moonquake slip directions because some moonquakes have reversed polarity waveforms; these moonquakes appear to slip “backwards”. We sought to determine whether this reversal arises because of a spatially varying tectonic

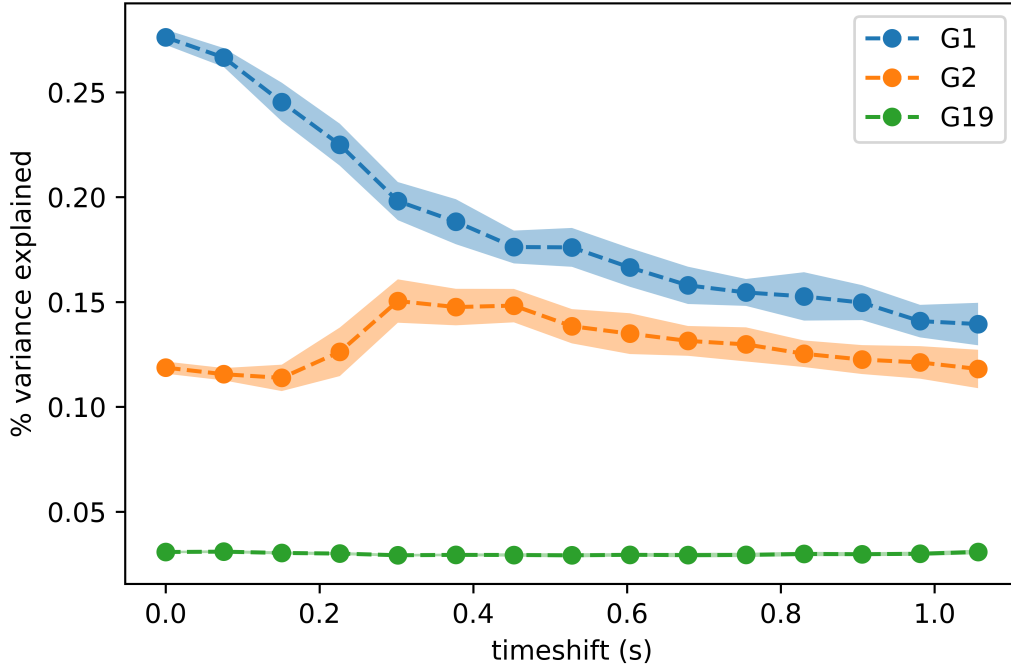


Figure 9. Testing the influence of inaccurate waveform alignment. We apply random time-shifts with magnitude up to 1.1s (x-axis) and determine the percentage of the data variance explained by the first (blue), second (orange), and nineteenth (green) principal components.

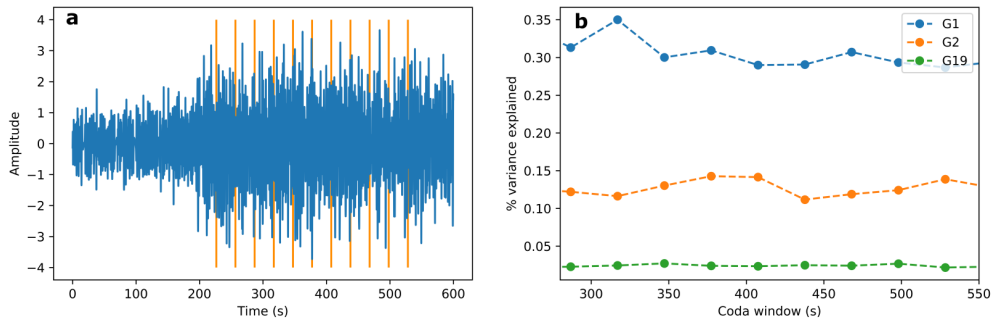


Figure 10. a) A single moonquake waveform, observed at station S12 in flat mode, divided (orange lines) into 30s windows throughout the coda, starting after the high-amplitude S wave arrival. b) Percentage variance accommodated by the first, second and last components in each time window. The variance percentages remain roughly constant as we move from the direct arrival into the more scattered coda. Scattering thus does not appear to explain the significant signal in the second component.

416 stress, where stress changes direction on either side of a plug (Figure 1b), or whether the
 417 reversal arises because the tectonic stress is small, and a tidal stress drives moonquakes
 418 and changes direction through time (Figure 1c). To distinguish between these models,
 419 we note that the tectonically driven plug model implies only one slip direction: forwards
 420 or backwards, while the tidal stress model could allow two slip directions: any combi-
 421 nation of forwards, backwards, left, or right. Our observation of two slip directions is more
 422 consistent with the tidal model of reversed polarity waveforms.

423 In principle, however, the plug model could also allow two slip directions. If the
 424 two sides of the plug are not parallel, we might see one slip direction (A) on one side of
 425 the plug and another direction (B) on the other side. In this case though, the two slip
 426 directions would be fixed. Slip might occur in direction A and in direction B, but not
 427 in any direction along the plane that contains directions A and B. For such a scenario,
 428 we could expect the estimated slip coefficient vectors, $[m_1, m_2]$, as decomposed using prin-
 429 cipal component analysis, to cluster around two directions, representing slip directions
 430 A and B on either side of the plug. We do not observe that clustering.

431 Instead, we see variation in the first and second slip coefficients (Figure 8). That
 432 2-D variation is more consistent with the tidal model, which allows the slip direction to
 433 move along the fault plane as the tidal stress changes.

434 The variation in the slip direction we observe is also consistent with P/S ampli-
 435 tude variations (Nakamura, 1978) and changes in the slip direction determined from S
 436 wave polarities (Koyama & Nakamura, 1980), all of which suggest slip occurs on a fixed
 437 fault plane, but the direction of slip can vary with time.

438 The two slip directions we identify thus suggest that an oscillating tidal stress drives
 439 deep moonquakes in the A01 nest and that this tidal stress changes the local stress di-
 440 rection through time.

441 **7.2 Implications of a small tectonic stress**

442 If tidal loading changes the direction of stress in the moonquake region through time,
 443 the tidal stresses must be larger than the local tectonic stress. We thus have a new con-
 444 straint on the magnitude of the tectonic stress at depth; it must be less than the max-
 445 imum modelled tidal stress of ~ 0.1 MPa (Toksöz et al., 1977; Minshull & Goulety, 1988;
 446 Weber et al., 2009).

447 **7.2.1 Excluding a ductile mechanism for moonquakes?**

448 We may use this cap on the tectonic stress to help constrain the enigmatic mech-
 449 anism of deep moonquakes under high pressures and temperatures. Some models have
 450 suggested that moonquake slip is driven by a viscous thermal runaway (Thielmann et
 451 al., 2015). As the fault slips, the temperature increases, grains reduce in size, and melt-
 452 ing can occur, localising and accelerating the slip on the fault. The runaway process al-
 453 lows ductile failure on seismic timescales. However, large initial shear stresses (~ 100 MPa
 454 at high strain rates (Thielmann et al., 2015)) are required to initialise localisation, and
 455 those stresses are not compatible with our 0.1 MPa upper bound on the tidal and tec-
 456 tonic stress in the A01 moonquake region. This allows us to rule out this mechanism for
 457 deep moonquakes.

458 A variety of models remain to explain the rapid failure that creates moonquakes
 459 at high pressure and temperature, though all the models remain poorly tested. One model
 460 suggests that high pore fluid pressure could reduce the effective stress on faults at depth
 461 and enable deep moonquake faults to slip. The lunar interior is wetter than previously
 462 thought (Evans et al., 2014). However, it remains unclear whether there is enough wa-
 463 ter in the right places to account for the generation of deep moonquakes.

464 Alternatively, deep moonquakes could be related to a mineral phase change, as pro-
 465 posed for deep (> 400 km) earthquakes. However, current models of the lunar interior
 466 do not identify a suitable phase change (Garcia et al., 2012), and this phase change would
 467 have to somehow occur repeatedly to create repeating moonquakes in a small volume.

468 **7.2.2 Lunar interior**

469 In addition to improving our understating of the mechanism of deep moonquakes,
 470 our moonquake-derived stress bounds, which imply that the local tectonic stress is smaller
 471 than the tidal stress, also provide constraints on thermal and dynamic models of the lu-
 472 nar interior. This stress bound implies that any stress from thermal contraction must
 473 be less than 0.1 MPa, consistent with previous estimates (Solomon & Chaiken, 1976).
 474 We can also place an upper bound on any remaining convection. If we assume a New-
 475 tonian viscosity of 10^{21} Pa s (e.g., Li et al., 2019), a long term stress smaller the 0.1 MPa
 476 implies a local strain rate smaller than 10^{-16} s⁻¹. Future research may find other uses
 477 for our moonquake-derived stress bounds. For example, the bounds might be used to pro-
 478 vide constraints on stress concentrations around local heterogeneity within the lunar in-
 479 terior (Zhao et al., 2012; Qin et al., 2012; Sakamaki et al., 2010; Steinberger et al., 2015).

480 **7.3 Further application to moonquakes and earthquakes**

481 The methodology developed in this study may also be relevant for future work. We
 482 have applied the PCA methodology only to the A01 nest, but this technique could let
 483 us examine more moonquakes, as recorded in the Apollo data or in data collected by the
 484 new broadband seismometer on the Farside Seismic Suite package, expected to land on
 485 the far side of the Moon in 2024 or 2025.

486 The PCA method appears necessary on the Moon, but it could also be useful for
 487 events on Earth, particularly in situations where there is no clear first arrival or where
 488 network coverage is sparse.

489 **8 Conclusion**

490 In this work, we sought both to understand the origin of moonquakes that slip “back-
 491 wards” and to constrain the relative magnitudes of tidal and tectonic stresses deep in
 492 the lunar interior. Our observation of two slip directions implies that moonquakes’ re-
 493 versed polarity waveforms result from an oscillating tidal stress, which encourages moon-
 494 quakes to slip forwards, backwards, left, or right depending on the phase of the tide. To
 495 explain these varying slip directions, the tidal stresses, which have a magnitude around
 496 0.1 MPa (Toksöz et al., 1977; Minshull & Gouly, 1988; Weber et al., 2009), must be larger
 497 than the local tectonic stress. Our observations thus imply that the tectonic stress near
 498 the A01 nest, at 900 km depth, is less than 0.1 MPa. That small tectonic stress may be
 499 employed in future modelling of the lunar interior. Further, the small stress implies that
 500 viscous thermal runaway, which requires a large stress for initiation (Thielmann et al.,
 501 2015), is unlikely to explain the existence of deep moonquakes.

502 **Acknowledgments**

503 We gratefully acknowledge the availability of the long period Apollo seismic data from
 504 the IGP data centre (<http://datacenter.ipgp.fr/data.php>). We would like to thank Ceri
 505 Nunn and Taichi Kawamura for their useful insights on the Apollo seismic data. AT was
 506 supported by STFC studentship ST/S505626/1.

References

- 507
- 508 Araki, H. (2001). Focal processes of deep moonquakes. *Journal of the Geodetic Soci-*
 509 *ety of Japan*, 47(1), 508–513.
- 510 Bishop, C. M., & Nasrabadi, N. M. (2006). *Pattern recognition and machine learn-*
 511 *ing* (Vol. 4) (No. 4). Springer.
- 512 Brantut, N., Sulem, J., & Schubnel, A. (2011). Effect of dehydration reactions on
 513 earthquake nucleation: Stable sliding, slow transients, and unstable slip. *Jour-*
 514 *nal of Geophysical Research: Solid Earth*, 116(B5).
- 515 Bulow, R., Johnson, C., & Shearer, P. (2005). New events discovered in the apollo
 516 lunar seismic data. *Journal of Geophysical Research: Planets*, 110(E10).
- 517 Burnley, P. C., Green, H. W., & Prior, D. J. (1991). Faulting associated with the
 518 olivine to spinel transformation in mg2geo4 and its implications for deep-focus
 519 earthquakes. *Journal of Geophysical Research: Solid Earth*, 96(B1), 425–443.
- 520 Davies, J. H. (1999). The role of hydraulic fractures and intermediate depth earth-
 521 quakes in subduction zone magmatism. *Nature*, 398(6723), 142–145.
- 522 Dobson, D., Meredith, P., & Boon, S. (2002). Microseismicity associated with antig-
 523 orite dehydration: Laboratorysimulation of deep-focus earthquakes. In *Egs*
 524 *general assembly conference abstracts* (p. 3985).
- 525 Evans, A., Zuber, M., Weiss, B., & Tikoo, S. (2014). A wet, heterogeneous lunar
 526 interior: Lower mantle and core dynamo evolution. *Journal of Geophysical Re-*
 527 *search: Planets*, 119(5), 1061–1077.
- 528 Frohlich, C., & Nakamura, Y. (2009). The physical mechanisms of deep moonquakes
 529 and intermediate-depth earthquakes: How similar and how different? *Physics*
 530 *of the Earth and Planetary Interiors*, 173(3-4), 365–374.
- 531 Gaddes, M., Hooper, A., & Bagnardi, M. (2019). Using machine learning to auto-
 532 matically detect volcanic unrest in a time series of interferograms. *Journal of*
 533 *Geophysical Research: Solid Earth*, 124(11), 12304–12322.
- 534 Garcia, R. F., Gagnepain-Beyneix, J., Chevrot, S., & Lognonné, P. (2012). Erra-
 535 tum to “very preliminary reference moon model”, by rf garcia, j. gagnepain-
 536 beyneix, s. chevrot, p. lognonné [phys. earth planet. inter. 188 (2011) 96–113].
 537 *Physics of the Earth and Planetary Interiors*, 202, 89–91.
- 538 Green, H., & Burnley, P. (1989). A new self-organizing mechanism for deep-focus
 539 earthquakes. *Nature*, 341(6244), 733–737.
- 540 Hacker, B. R., Peacock, S. M., Abers, G. A., & Holloway, S. D. (2003). Subduction
 541 factory 2. are intermediate-depth earthquakes in subducting slabs linked to
 542 metamorphic dehydration reactions? *Journal of Geophysical Research: Solid*
 543 *Earth*, 108(B1).
- 544 Hardebeck, J. L., & Shearer, P. M. (2002). A new method for determining first-
 545 motion focal mechanisms. *Bulletin of the Seismological Society of America*,
 546 92(6), 2264–2276.
- 547 John, T., Medvedev, S., Rüpke, L. H., Andersen, T. B., Podladchikov, Y. Y., &
 548 Austrheim, H. (2009). Generation of intermediate-depth earthquakes by
 549 self-localizing thermal runaway. *Nature Geoscience*, 2(2), 137–140.
- 550 Karato, S.-i., Riedel, M. R., & Yuen, D. A. (2001). Rheological structure and de-
 551 formation of subducted slabs in the mantle transition zone: implications for
 552 mantle circulation and deep earthquakes. *Physics of the Earth and Planetary*
 553 *Interiors*, 127(1-4), 83–108.
- 554 Kawamura, T., Lognonné, P., Nishikawa, Y., & Tanaka, S. (2017). Evaluation of
 555 deep moonquake source parameters: Implication for fault characteristics and
 556 thermal state. *Journal of Geophysical Research: Planets*, 122(7), 1487–1504.
 557 doi: 10.1002/2016JE005147
- 558 Kelemen, P. B., & Hirth, G. (2007). A periodic shear-heating mechanism for
 559 intermediate-depth earthquakes in the mantle. *Nature*, 446(7137), 787–790.
- 560 Kirby, S. H. (1987). Localized polymorphic phase transformations in high-pressure
 561 faults and applications to the physical mechanism of deep earthquakes. *Journal*

- 562 of *Geophysical Research: Solid Earth*, 92(B13), 13789–13800.
- 563 Kirby, S. H., Stein, S., Okal, E. A., & Rubie, D. C. (1996). Metastable mantle phase
564 transformations and deep earthquakes in subducting oceanic lithosphere. *Re-*
565 *views of geophysics*, 34(2), 261–306.
- 566 Koyama, J., & Nakamura, Y. (1980). Focal mechanism of deep moonquakes. In *Lu-*
567 *nar and planetary science conference proceedings* (Vol. 11, pp. 1855–1865).
- 568 Lammlein, D. R. (1977). Lunar seismicity and tectonics. *Physics of the Earth and*
569 *Planetary Interiors*, 14(3), 224–273.
- 570 Li, H., Zhang, N., Liang, Y., Wu, B., Dygert, N. J., Huang, J., & Parmentier, E.
571 (2019). Lunar cumulate mantle overturn: A model constrained by ilmenite
572 rheology. *Journal of Geophysical Research: Planets*, 124(5), 1357–1378.
- 573 Maaten, L. v. d., & Hinton, G. (2008). Visualizing data using t-sne. *Journal of ma-*
574 *chine learning research*, 9(Nov), 2579–2605.
- 575 McInnes, L., Healy, J., & Astels, S. (2017). hdbscan: Hierarchical density based clus-
- 576 tering. *J. Open Source Softw.*, 2(11), 205.
- 577 Meade, C., & Jeanloz, R. (1991). Deep-focus earthquakes and recycling of water into
578 the earth’s mantle. *Science*, 252(5002), 68–72.
- 579 Minshull, T., & Gouly, N. (1988). The influence of tidal stresses on deep moon-
- 580 quake activity. *Physics of the earth and planetary interiors*, 52(1-2), 41–55.
- 581 Nakamura, Y. (1978). A1 moonquakes-source distribution and mechanism. In *Lunar*
582 *and planetary science conference proceedings* (Vol. 9, pp. 3589–3607).
- 583 Nakamura, Y. (2003). New identification of deep moonquakes in the apollo lunar
584 seismic data. *Physics of the Earth and Planetary Interiors*, 139(3-4), 197–205.
- 585 Nakamura, Y. (2005). Spatial extent of a deep moonquake nest—a preliminary re-
- 586 port of reexamination. In *36th annual lunar and planetary science conference*
587 (p. 1168).
- 588 Nunn, C., Garcia, R. F., Nakamura, Y., Marusiak, A. G., Kawamura, T., Sun, D.,
589 ... others (2020). Lunar seismology: a data and instrumentation review. *Space*
590 *Science Reviews*, 216(5), 1–39.
- 591 Nunn, C., Nakamura, Y., & Igel, H. (2017). Apollo passive seismic experiments:
592 lunar data in seed format. In *Agu fall meeting abstracts* (Vol. 2017, pp. P41D–
593 2860).
- 594 Nunn, C., Weber, R. C., & Panning, M. (2020). Improving the accessibility of the
595 apollo seismic data: Archiving at iris and the pds. In *Lunar and planetary sci-*
596 *ence conference* (p. 2269).
- 597 Ogawa, M. (1987). Shear instability in a viscoelastic material as the cause of deep
598 focus earthquakes. *Journal of Geophysical Research: Solid Earth*, 92(B13),
599 13801-10.
- 600 Proctor, B., & Hirth, G. (2015). Role of pore fluid pressure on transient strength
601 changes and fabric development during serpentine dehydration at mantle con-
602 ditions: Implications for subduction-zone seismicity. *Earth and Planetary*
603 *Science Letters*, 421, 1–12.
- 604 Qin, C., Muirhead, A. C., & Zhong, S. (2012). Correlation of deep moonquakes and
605 mare basalts: Implications for lunar mantle structure and evolution. *Icarus*,
606 220(1), 100–105. doi: 10.1016/j.icarus.2012.04.023
- 607 Sakamaki, T., Ohtani, E., Urakawa, S., Suzuki, A., Katayama, Y., & Zhao, D.
608 (2010). Density of high-ti basalt magma at high pressure and origin of hetero-
- 609 geneities in the lunar mantle. *Earth and Planetary Science Letters*, 299(3-4),
610 285–289.
- 611 Schubnel, A., Brunet, F., Hilairret, N., Gasc, J., Wang, Y., & Green, H. W. (2013).
612 Deep-focus earthquake analogs recorded at high pressure and temperature in
613 the laboratory. *Science*, 341(6152), 1377–1380.
- 614 Solomon, S., & Chaiken, J. (1976). Thermal expansion and thermal stress in the
615 moon and terrestrial planets-clues to early thermal history. In *Lunar and plan-*
616 *etary science conference proceedings* (Vol. 7, pp. 3229–3243).

- 617 Steinberger, B., Zhao, D., & Werner, S. C. (2015). Interior structure of the moon:
 618 constraints from seismic tomography, gravity and topography. *Physics of the*
 619 *Earth and Planetary Interiors*, *245*, 26–39.
- 620 Thielmann, M. (2018). Grain size assisted thermal runaway as a nucleation mech-
 621 anism for continental mantle earthquakes: Impact of complex rheologies.
 622 *Tectonophysics*, *746*, 611–623.
- 623 Thielmann, M., Rozel, A., Kaus, B., & Ricard, Y. (2015). Intermediate-depth earth-
 624 quake generation and shear zone formation caused by grain size reduction and
 625 shear heating. *Geology*, *43*(9), 791–794.
- 626 Toksöz, M. N., Goins, N. R., & Cheng, C. (1977). Moonquakes: Mechanisms and re-
 627 lation to tidal stresses. *Science*, *196*(4293), 979–981.
- 628 Weber, R. C., Bills, B., & Johnson, C. (2009). Constraints on deep moonquake focal
 629 mechanisms through analyses of tidal stress. *Journal of Geophysical Research:*
 630 *Planets*, *114*(E5).
- 631 Weber, R. C., Bills, B. G., & Johnson, C. L. (2010). A simple physical model for
 632 deep moonquake occurrence times. *Physics of the Earth and Planetary Interi-*
 633 *ors*, *182*(3-4), 152–160. doi: 10.1016/j.pepi.2010.07.009
- 634 White, R. S., Drew, J., Martens, H. R., Key, J., Soosalu, H., & Jakobsdóttir, S. S.
 635 (2011). Dynamics of dyke intrusion in the mid-crust of iceland. *Earth and*
 636 *Planetary Science Letters*, *304*(3-4), 300–312.
- 637 Yang, W., Hauksson, E., & Shearer, P. M. (2012). Computing a large refined catalog
 638 of focal mechanisms for southern california (1981–2010): Temporal stability of
 639 the style of faulting. *Bulletin of the Seismological Society of America*, *102*(3),
 640 1179–1194.
- 641 Zhao, D., Arai, T., Liu, L., & Ohtani, E. (2012). Seismic tomography and geochem-
 642 ical evidence for lunar mantle heterogeneity: comparing with earth. *Global and*
 643 *Planetary Change*, *90*, 29–36.